Towards a comprehensive delineation of white matter tract-related deformation

Zhou Zhou,[1†*] Xiaogai Li,[2†] Yuzhe Liu,[1] Madelen Fahlstedt,[2] Marios Georgiadis,[3] Xianghao Zhan,[1] Samuel J. Raymond,[1] Gerald Grant,[4,5] Svein Kleiven,[2‡] David Camarillo,[1,5,6‡] Michael Zeineh[3‡*]

[1] Department of Bioengineering, Stanford University, Stanford, CA, 94305, USA.
[2] Neuronic Engineering, KTH Royal Institute of Technology, Stockholm, 14152, Sweden.
[3] Department of Radiology, Stanford University, Stanford, CA, 94305, USA.
[4] Department of Neurosurgery, Stanford University, Stanford, CA, 94305, USA.
[5] Department of Neurology, Stanford University, Stanford, CA, 94305, USA.
[6] Department of Mechanical Engineering, Stanford University, Stanford, CA, 94305, USA.

[*] Corresponding author. Email: zhouz@stanford.edu, mzeineh@stanford.edu
[†] These authors contributed equally to this work.
[‡] These authors share senior authorship.

Author information:

Zhou Zhou, Department of Bioengineering, Stanford University, Stanford, CA, 94305, USA, Email:zhouz@stanford.edu

Xiaogai Li, Division of Neuronic Engineering, Royal Institute of Technology (KTH), SE-14152, Huddinge, Sweden, Email: xiaogai@kth.se

Yuzhe Liu, Department of Bioengineering, Stanford University, Stanford, CA, 94305, USA, Email: yuzheliu@stanford.edu

Madelen Fahlstedt, Division of Neuronic Engineering, Royal Institute of Technology (KTH), SE-14152, Huddinge, Sweden, Email: madelenf@kth.se

Marios Georgiadis, Department of Radiology, Stanford University, 213 Quarry Road, Stanford, CA 94305, USA, Email: mariosg@stanford.edu

Xianghao Zhan, Department of Bioengineering, Stanford University, Stanford, CA, 94305, USA, Email: xzhan96@stanford.edu

Samuel J. Raymond, Department of Bioengineering, Stanford University, Stanford, CA, 94305, USA, Email: sjray@stanford.edu

Gerald Grant, Department of Neurosurgery, Stanford University School of Medicine, 291 Campus Drive, Stanford, CA 94305, Stanford, CA. Email: ggrant2@stanford.edu

Svein Kleiven, Division of Neuronic Engineering, Royal Institute of Technology (KTH), SE-14152, Huddinge, Sweden, Email: sveink@kth.se

David Camarillo, Department of Bioengineering, Stanford University, 443 Via Ortega, Room 202, Stanford, CA, 94305, Email: dcamarillo@stanford.edu

Michael Zeineh, Department of Radiology, Stanford University, 213 Quarry Road, Stanford, CA 94305, USA, Email: mzeineh@stanford.edu

Abstract

Finite element (FE) models of the human head are valuable instruments to explore the mechanobiological pathway from external loading, localized brain response, and resultant injury risks. The injury predictability of these models depends on the use of effective criteria as injury predictors. The FE-derived normal deformation along white matter (WM) fiber tracts (i.e., tract-oriented strain) has recently been suggested as an appropriate predictor for axonal injury. However, the tract-oriented strain only represents a partial depiction of the WM fiber tract deformation. A comprehensive delineation of tract-related deformation may improve the injury predictability of the FE head model by delivering new tract-related criteria as injury predictors. Thus, the present study performed a theoretical strain analysis to comprehensively characterize the WM fiber tract deformation by relating the strain tensor of the WM element to its embedded fiber tracts. Three new tract-related strains were proposed, measuring the normal deformation vertical to the fiber tracts (i.e., tract-vertical strain), and shear deformation along and vertical to the fiber tracts (i.e., axial-shear strain and lateral-shear strain, respectively). The injury predictability of these three newly-proposed strain peaks along with the previously-used tract-oriented strain peak and maximum principal strain (MPS) were evaluated by simulating 151 impacts with known outcome (concussion or no-concussion). The results showed that four tract-related strain peaks exhibit superior performance compared to MPS in discriminating concussion and non-concussion cases. This study presents a comprehensive quantification of WM tract-related deformation and advocates the use of orientation-dependent strains as criteria for injury prediction, which may ultimately contribute to an advanced mechanobiological understanding and enhanced computational predictability of brain injury.

Keywords

Axonal injury, Tract-related deformation, Injury criteria, Finite element analysis, Computational brain modelling

Highlight

- Deformation of white matte fiber tracts is directly related to brain injury, but only partially analyzed thus far.
- A theoretical derivation that comprehensively characterizes white matter tract-related deformation is conducted.
- Analytical formulas of three novel tract-related strains are presented.
- Tract-related strain peaks are better predictors for concussion than the maximum principal strain.

Introduction

Traumatic brain injury (TBI) is a growing public health concern worldwide. In the United States, the number of TBI-related victims in 2013 is estimated to be 2.8 million, resulting in 2.5 million emergency department visits, 282000 hospitalizations, and 56000 deaths [1]. A meta-analysis of injury data from 16 European countries reported an overall TBI incidence rate of 262 per 100000 and an average fatality rate of 11 per 100000 [2]. Olesen et al. [3] estimated a total cost of 33 billion Euros associated with TBI in 2010 in Europe. Despite global endeavors to prevent the occurrence and alleviate the consequence of TBI, neither a clear decrease in TBI-induced mortality nor improvement of overall outcome has been observed [4]. This is particularly true for axonal injury, which is notoriously underreported [5], difficult to diagnose [6], and associated with immediate and persistent impairment to attention and cognition [7]. This TBI-related urgency indicates that the current understanding of TBI pathogenesis is insufficient and cannot provide solid guidance for the development of head protection strategies and therapeutic tactics.

As numerical surrogates, finite element (FE) models of the human head have been increasingly used to explore the mechanobiological pathway from external loading, localized brain response, and resultant injury risk. The injury predictability of such numerical surrogates requires accurate anatomical and mechanical representations of each intracranial structure, precise descriptions of the interaction among various intracranial components, and appropriate criteria as injury predictors [8]. In part by using advanced neuroimaging techniques, it is feasible for current FE models to incorporate a high degree of structural detail. For example, several three-dimensional (3D) models possess a sophisticated anatomical depiction of the lateral ventricles [9, 10] and the skull [11, 12], by leveraging magnetic resonance imaging (MRI) and computed tomography scans, respectively. In parallel, persistent endeavors in experimental characterization of biological tissue guide the establishment of constitutive equations for numerical implementation. Recently, Mihai et al. [13] presented a family of hyperelastic models with material constants calibrated against the experimental curves of brain tissue under finite simple shear superposed on varying axial tension or

compression [14]. Emerging improvement has also been noted in the modeling of intracranial interfaces, especially for the fluid-structure interaction (FSI) scenarios. Recently, arbitrary Lagrange-Eulerian and smoothed particle hydrodynamics were respectively employed to emulate the brain-skull interface and brain-ventricle interface, contributing to an enhanced representation of the intracranial fluid dynamics [15-17]. However, contemporary head models appear to lack comparable explorations of the different aspects of brain injury criteria.

Great disparities exist between models when interpreting the estimated responses by means of injury criteria. Various measures characterizing the local mechanical responses of brain tissue have been derived from the computational studies to assess brain injury risk, such as intracranial pressure [18], stress [19, 20], strain [21], etc. Even when limited to strain-based metrics, the adopted criteria vary from maximum principal strain (MPS) [22], maximum shear strain [23], to strain-based derivatives (e.g., strain rate [24], the product of strain and strain rate [25], and cumulative strain damage measure (CSDM) [26]). No consensus has been reached yet on the best metric to describe tissue deformation and discriminate the injury severity. Considering that axonal injury is a type of trauma in which diffuse lesions occur within fiber tracts usually consisting of oriented axons, any measures that account for the orientation of fiber tracts are anatomically relevant and may function as promising candidate criteria. White matter (WM) fiber orientation and distribution from larger bundles can be derived from an MRI technique called diffusion tensor imaging (DTI) [27]. In DTI, the fiber orientation distribution in each voxel is represented by a rank-2 symmetric tensor, visually depicted by an ellipsoid [28]. Recent studies have integrated the orientation information of fiber tract delineated by DTI in the FE model in order to extract the deformation pertaining to fiber tracts [9, 25, 29-50]. Across these numerical endeavors, a specific component, i.e., tract-oriented strain measuring the normal deformation along the WM fiber tracts, was extracted by resolving the strain tensor along the fiber orientation. Of note, the tract-oriented strain is synonymous with axonal strain or fiber strain [38, 43, 45]. It has been repeatedly reported by several independent groups that the

maximum tract-oriented strain exhibited improved injury predictability than MPS [25, 38, 40, 41, 47, 50].

Despite the inspiring initial results, the tract-oriented strain only represents a partial depiction of WM fiber tract deformation along the fiber tracts. From a mathematical perspective, projecting the deformation (described by a strain tensor) along the fiber orientation to attain the tract-oriented strain (described by a scalar) discards a large amount of information originally conveyed by the strain tensor. A comprehensive delineation of tract-related deformation that appropriately utilizes the full information of the strain tensor may hold the potential to further improve injury predictability of FE models. Such potential is supported by the findings of *in vitro* models [51-54]. For example, through spatiotemporal correlation between neurite pathomorphology and the deformation of neurons, Bar-Kochba et al. [51] found that bleb formation was strongly correlated with shearing along the longitudinal direction of neurons, while the timeframe of neuronal death was related to the integral of the stretching over the length of the neuron. Nakadate et al. [54] delivered uniaxial stretching to a two-dimensional (2D) culture slice with randomly oriented axons and noted swellings in axons with their orientations exhibiting various angles relative to the stretching direction. Based on the above analyses, any criteria related to the deformation of WM axonal fibers may be candidate predictors for axonal injury, the full array of which have yet to be properly considered in FE head models.

The aim of this study is to present a comprehensive delineation of WM fiber tract deformation and investigate the injury predictability of novel tract-related strain metrics. To achieve this, a theoretical strain analysis was performed by relating the strain tensor of the WM element to its embedded fiber tracts. In addition to the previously proposed tract-oriented strain, three new tract-related strain measures were presented, characterizing the normal deformation vertical (e.g., perpendicular) to the fiber tracts, and shear deformation along and vertical to the fiber tracts, respectively. The injury predictability of these three newly-proposed strain peaks was evaluated by simulating 151 impacts with known outcome (concussion or no-concussion) and compared to the

previously used maximum tract-oriented strain and MPS. We hypothesize that the four tract-related strain peaks exhibit superior injury predictability than MPS.

Methods

Finite element head model

The FE model (Fig. 1) used in this study was previously developed at the Royal Institute of Technology (KTH) in Stockholm [22] using the LS-DYNA software. Responses of the model have shown good correlations with experiments of brain-skull relative motion [55, 56], intracranial pressure [57], and brain strain [58]. As shown in Fig. 1, the model includes the scalp, skull, brain, subarachnoid cerebrospinal fluid (CSF), ventricles, dura mater, falx, tentorium, pia mater, eleven pairs of the largest parasagittal bridging veins, and a simplified neck with the extension of the spinal cord. Anatomical differentiation was implemented to divide brain elements into cerebral gray matter (GM), cerebral WM, corpus callosum, thalamus, brainstem, midbrain, and cerebellum (Fig. 1B-C). Detailed information regarding the geometry discretization and material choice for each head component, as well as interface conditions among various intracranial structures, are available in previous studies [15, 22]. Particularly, because of the lack of consensus regarding the mechanical anisotropy and heterogeneity of the brain [59, 60], the brain was simulated as a homogeneous and isotropic medium with its nonlinear behavior described by a second-order hyperelastic constitutive law with additional linear viscoelastic terms to account for its rate dependence [22].

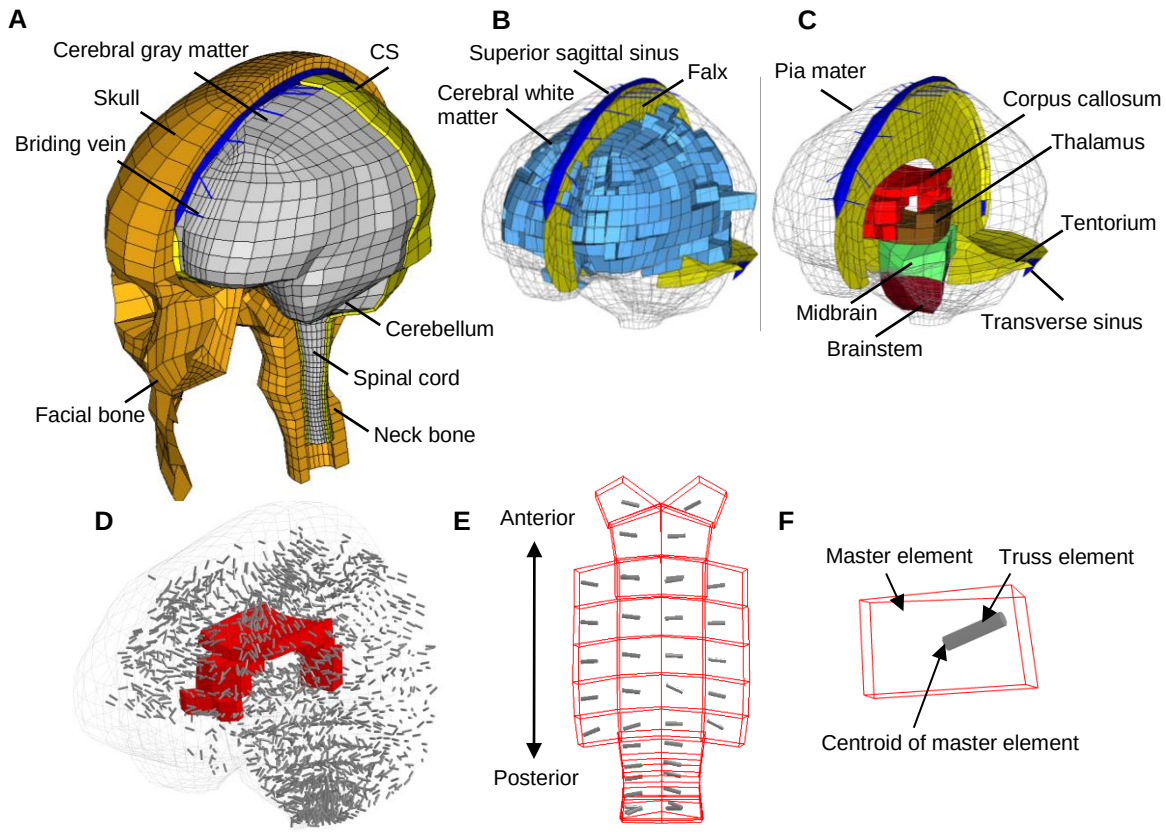

Fig. 1. Finite element model of the human head with embedded truss elements. (A) Finite element model of the human head with the skull open to expose the CSF and brain. (B) Model of cerebral white matter, superior sagittal sinus, and falx. (C) Model of deep brain structures, pia mater, tentorium, and transverse sinus. (D) Brain with embedded truss elements representing the dynamically-changing local fiber orientation, and the corpus callosum elements in red. (F) Top view of the truss elements within the corpus callosum. (E) A representative element in the corpus callosum with a truss element embedded.

Embedded element method for real-time fiber orientation

Given that the deformation of WM fiber tracts is directly dependent on the real-time fiber orientation, an embedded element method was implemented in the FE model to monitor the temporal evaluation of fiber orientation (Fig. 1D-F) following the approach presented earlier [49]. Briefly, the brain mesh of the head model was voxelized to generate a reference volume, which was aligned to the volume of the ICBM DTI-81 atlas [27] via an affine registration. For each WM element in the head model, corresponding voxels in the DTI atlas exhibiting spatial alignment with the given WM element were identified, and the diffusion tensors of these identified voxels were resampled to obtain the average fiber orientation. The DTI-derived average fiber orientation was concretely represented by truss elements (serving as slave elements), which were embedded within the WM elements (serving as master elements). Note that the embedded truss elements only served as

auxiliaries for obtaining the updated orientation of fiber tracts at each time step without additional contribution to mechanical stiffness. For a given truss element, one node was located at the centroid of its master element, while the other fell within the boundary of its master element (Fig. 1F). Both acceleration and velocity of a given truss element were determined exclusively by its master element without relative motion between them. Consequently, the real-time fiber orientation during head impacts was reflected by the temporal direction of the truss element and was updated at each timestep of the simulation. Details regarding the coupling protocol between DTI and WM element and the implementation of the embedded element method for tracking the real-time fiber orientation are available in [37] and [49], respectively.

Derivation of tract-related strains via coordinate transformations

To decipher WM fiber tract-related deformation, a theoretical strain analysis was performed via coordinate transformations [61], in which the strain tensor of WM element was transformed to the coordinate systems with one axis aligned with the real-time fiber orientation. As illustrated in Fig. 2, both the Green-Lagrange strain tensor for a representative WM element and the orientation of its embedded truss element for a given timestep were extracted from a pre-computed simulation and then transformed into the skull-fixed coordinate system ($\boldsymbol{XYZ}$) (Fig. 2B) with $\boldsymbol{X} = [1 \quad 0 \quad 0]^T$, $\boldsymbol{Y} = [0 \quad 1 \quad 0]^T$, and $\boldsymbol{Z} = [0 \quad 0 \quad 1]^T$. The strain tensor and the fiber orientation within the skull-fixed coordinate system are denoted as $\boldsymbol{E}_{\text{skull}}$ and $\boldsymbol{v}$. The $\boldsymbol{v}$ is a unit vector with its three components along the $\boldsymbol{X}$, $\boldsymbol{Y}$, and $\boldsymbol{Z}$ axes as v_1, v_2, and v_3, respectively. Details about the transformation of the strain tensor from the global coordinate system to the skull-fixed coordinate system are available in the previous publications from our group [42, 49] as well as others [25].

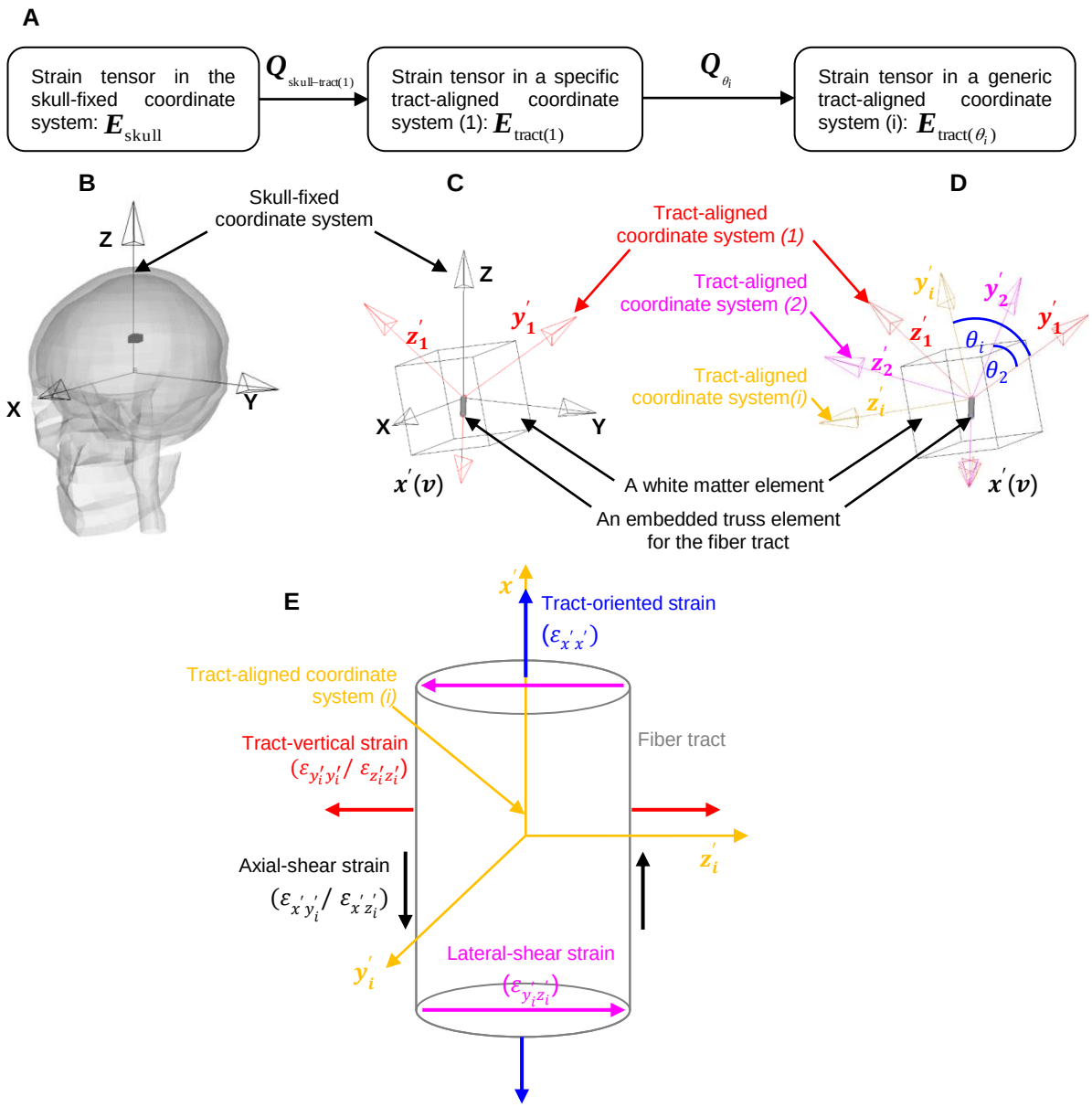

Fig. 2. Demonstration of coordinate systems used in the theoretical analysis via the coordinate transformations to delineate the tract-related deformation for one representative element at one timestep. (A) Summary of the coordinate transformations of the strain tensor illustrated in subfigure (B)-(D). (B) An FE model of the human head with a representative white matter element highlighted in dark gray. A skull-fixed coordinate system and corresponding axes are illustrated with the origin at the head's center of gravity. (C) A representative white matter element with an embedded truss element representing the tract orientation. A modified skull-fixed coordinate system with the origin at the centroid of the white matter element and a specific tract-aligned coordinate system (1) is superimposed. (D) A generic tract-aligned coordinate system with the x'axis aligned with the real-time tract orientation. (E) Definition of tract-related strains with respect to the fiber tract in the tract-aligned coordinate system (*i*).

Given that the deformation of the fiber tracts is dependent on the fiber orientation, a specific tract-aligned coordinate system, i.e., the tract-aligned coordinate system (*1*) ($x'y_1'z_1'$) in Fig. 2C, was established with the origin at the centroid of the WM element and the x' aligned with the

$\boldsymbol{v}$. The $\boldsymbol{y}_1^{'}$ was computed as the cross product of $\boldsymbol{x}^{'}$ and $\boldsymbol{X}$, while the $\boldsymbol{z}_1^{'}$ as the cross product of $\boldsymbol{x}^{'}$ and $\boldsymbol{y}_1^{'}$.

$$\boldsymbol{x}^{'} = \boldsymbol{v} = \begin{bmatrix} v_1 \\ v_2 \\ v_3 \end{bmatrix} \quad \boldsymbol{y}_1^{'} = \boldsymbol{x}^{'} \times \boldsymbol{X} = \frac{1}{\sqrt{v_2^2 + v_3^2}} \begin{bmatrix} 0 \\ -v_3 \\ -v_2 \end{bmatrix} \quad \boldsymbol{z}_1^{'} = \boldsymbol{x}^{'} \times \boldsymbol{y}_1^{'} = \frac{1}{\sqrt{(v_2^2 + v_3^2)}} \begin{bmatrix} v_2^2 + v_3^2 \\ -v_1 v_2 \\ -v_1 v_3 \end{bmatrix} \tag{1-3}$$

The strain tensor within the tract-aligned coordinate system (*1*), denoted by $\boldsymbol{E}_{\text{tract(1)}}$, can be calculated as

$$\boldsymbol{E}_{\text{tract(1)}} = \boldsymbol{Q}_{\text{skull-tract(1)}} \boldsymbol{E}_{\text{skull}} \boldsymbol{Q}^T_{\text{skull-tract(1)}} = \begin{bmatrix} \varepsilon_{x^{'}x^{'}} & \varepsilon_{x^{'}y_1^{'}} & \varepsilon_{x^{'}z_1^{'}} \\ \varepsilon_{x^{'}y_1^{'}} & \varepsilon_{y_1^{'}y_1^{'}} & \varepsilon_{y_1^{'}z_1^{'}} \\ \varepsilon_{x^{'}z_1^{'}} & \varepsilon_{y_1^{'}z_1^{'}} & \varepsilon_{z_1^{'}z_1^{'}} \end{bmatrix} \tag{4}$$

with the $\boldsymbol{Q}_{\text{skull-tract(1)}}$ given by

$$\boldsymbol{Q}_{\text{skull-tract(1)}} = \begin{bmatrix} \cos(\boldsymbol{x}^{'}, \boldsymbol{X}) & \cos(\boldsymbol{x}^{'}, \boldsymbol{Y}) & \cos(\boldsymbol{x}^{'}, \boldsymbol{Z}) \\ \cos(\boldsymbol{y}_1^{'}, \boldsymbol{X}) & \cos(\boldsymbol{y}_1^{'}, \boldsymbol{Y}) & \cos(\boldsymbol{y}_1^{'}, \boldsymbol{Z}) \\ \cos(\boldsymbol{z}_1^{'}, \boldsymbol{X}) & \cos(\boldsymbol{z}_1^{'}, \boldsymbol{Y}) & \cos(\boldsymbol{z}_1^{'}, \boldsymbol{Z}) \end{bmatrix} = \begin{vmatrix} v_1 & v_2 & v_3 \\ 0 & \frac{-v_3}{\sqrt{(v_2^2 + v_3^2)}} & \frac{v_2}{\sqrt{(v_2^2 + v_3^2)}} \\ \sqrt{(v_2^2 + v_3^2)} & \frac{-v_1 v_2}{\sqrt{(v_2^2 + v_3^2)}} & \frac{-v_1 v_3}{\sqrt{(v_2^2 + v_3^2)}} \end{vmatrix} \tag{5}$$

Since $\boldsymbol{E}_{\text{skull}}$, v_1, E_{skull}, and v_3 were output from LS-DYNA solver, all components of $\boldsymbol{E}_{\text{tract(1)}}$ were known variables.

Within the context of having the $\boldsymbol{x}^{'}$ aligned with the $\boldsymbol{v}$, the $\boldsymbol{x}^{'}$ was unique and the orthonormal unit vectors $\boldsymbol{y}_1^{'}$ and $\boldsymbol{z}_1^{'}$ were instead non-unique. For all the components in the strain tensor, only $\varepsilon_{x^{'}x^{'}}$ was exclusively dependent on the $\boldsymbol{x}^{'}$, and, thus, can be obtained as

$$\varepsilon_{x^{'}x^{'}} = \boldsymbol{v}^T \cdot \boldsymbol{E}_{\text{skull}} \cdot \boldsymbol{v} \tag{6}$$

As depicted in Fig. 2E, $\varepsilon_{x'x'}$ is referred to as tract-oriented strain, characterizing the normal deformation along fiber tracts. The tract-oriented strain has been similarly extracted in previous studies [9, 25, 29-50].

For the remaining components in the transformed strain tensor, whose magnitudes are affected by the choice of $\boldsymbol{y}_1^{'}$ and $\boldsymbol{z}_1^{'}$, a generic tract-aligned coordinate system, i.e., the tract-aligned coordinate system (*i*) ($\boldsymbol{x}^{'}\boldsymbol{y}_i^{'}\boldsymbol{z}_i^{'}$) was introduced (Fig. 2D). In the generic tract-aligned coordinate system (*i*), the $\boldsymbol{x}^{'}$ remained aligned with the $\boldsymbol{V}$, while the orthonormal unit vectors $\boldsymbol{y}_i^{'}$ and $\boldsymbol{z}_i^{'}$ were arbitrarily established within the plane defined by $\boldsymbol{y}_1^{'}$ and $\boldsymbol{z}_1^{'}$. To quantify the angle between $\boldsymbol{y}_1^{'}$ and $\boldsymbol{y}_i^{'}$ (equivalent to the angle between the $\boldsymbol{z}_1^{'}$ and $\boldsymbol{z}_i^{'}$), a new variable, θ_i, was introduced (Fig. 2D). Thus, the strain tensor within the tract-aligned coordinate system (*i*) ($\boldsymbol{E}_{\text{tract}(\theta_i)}$) can be calculated as

$$\boldsymbol{E}_{\text{tract}\,(\theta_i)} = \boldsymbol{Q}_{\theta_i}\boldsymbol{E}_{\text{tract}(1)}\boldsymbol{Q}_{\theta_i}^{T} = \begin{bmatrix} \varepsilon_{x'x'} & \varepsilon_{x'y_i'} & \varepsilon_{x'z_i'} \\ \varepsilon_{x'y_i'} & \varepsilon_{y_i'y_i'} & \varepsilon_{y_i'z_i'} \\ \varepsilon_{x'z_i'} & \varepsilon_{y_i'z_i'} & \varepsilon_{z_i'z_i'} \end{bmatrix} \tag{7}$$

with the $\boldsymbol{Q}_{\theta_i}$ given by

$$\boldsymbol{Q}_{\theta_i} = \begin{bmatrix} \cos(\boldsymbol{x}^{'},\boldsymbol{x}^{'}) & \cos(\boldsymbol{x}^{'},\boldsymbol{y}_i^{'}) & \cos(\boldsymbol{x}^{'},\boldsymbol{z}_i^{'}) \\ \cos(\boldsymbol{y}_i^{'},\boldsymbol{x}^{'}) & \cos(\boldsymbol{y}_i^{'},\boldsymbol{y}_i^{'}) & \cos(\boldsymbol{y}_i^{'},\boldsymbol{z}_i^{'}) \\ \cos(\boldsymbol{z}_i^{'},\boldsymbol{x}^{'}) & \cos(z_i^{'},\boldsymbol{y}_i^{'}) & \cos(\boldsymbol{z}_i^{'},\boldsymbol{z}_i^{'}) \end{bmatrix} = \begin{bmatrix} 1 & 0 & 0 \\ 0 & \cos\theta_i & -\sin\theta_i \\ 0 & \sin\theta_i & \cos\theta_i \end{bmatrix} \tag{8}$$

where $0^{\circ} \le \theta_i \le 360^{\circ}$.

Integrating the equation (4) and equation (8) into equation (7), all components in $\boldsymbol{E}_{\text{tract}(\theta_i)}$ can be obtained as a function of θ_i.

$$\varepsilon_{y_i'y_i'}(\theta_i) = \frac{\varepsilon_{y_1'y_1'} + \varepsilon_{z_1'z_1'}}{2} - \sqrt{\left(\frac{\varepsilon_{y_1'y_1'} - \varepsilon_{z_1'z_1'}}{2}\right)^2 + \varepsilon_{y_1'z_1'}^2}\,\sin(2\theta_i + \phi_1)$$

(9)

where $\phi_1 = \arctan(\frac{\varepsilon_{y_1'y_1'} - \varepsilon_{z_1'z_1'}}{2\varepsilon_{y_1'z_1'}})$.

$$\varepsilon_{z_i'z_i'}(\theta_i) = \frac{\varepsilon_{y_1'y_1'} + \varepsilon_{z_1'z_1'}}{2} + \sqrt{(\frac{\varepsilon_{y_1'y_1'} - \varepsilon_{z_1'z_1'}}{2})^2 + \varepsilon_{y_1'z_1'}^2}\ \sin(2\theta_i + \phi_2) \tag{10}$$

where $\phi_2 = \arctan(\frac{\varepsilon_{z_1'z_1'} - \varepsilon_{y_1'y_1'}}{2\varepsilon_{y_1'z_1'}})$.

$$\varepsilon_{x'y_i'}(\theta_i) = -\sqrt{\varepsilon_{x'y_1'}^2 + \varepsilon_{x'z_1'}^2}\ \sin(\theta_i + \phi_3) \tag{11}$$

where $\phi_3 = \arctan(-\frac{\varepsilon_{x'z_1'}}{\varepsilon_{x'y_1'}})$.

$$\varepsilon_{x'z_i'}(\theta_i) = \sqrt{\varepsilon_{x'y_1'}^2 + \varepsilon_{x'z_1'}^2}\ \sin(\theta_i + \phi_4) \tag{12}$$

where $\phi_4 = \arctan(\frac{\varepsilon_{x'y_1'}}{\varepsilon_{x'z_1'}})$.

$$\varepsilon_{y_i'z_i'}(\theta_i) = \sqrt{(\frac{\varepsilon_{y_1'y_1'} - \varepsilon_{z_1'z_1'}}{2})^2 + \varepsilon_{y_1'z_1'}^2}\ \sin(2\theta_i + \phi_5) \tag{13}$$

where $\phi_5 = \arctan(\frac{2\varepsilon_{y_1'z_1'}}{\varepsilon_{y_1'y_1'} - \varepsilon_{z_1'z_1'}})$.

Note that $\varepsilon_{x'x'}$ is exclusively dependent on the choice of $\boldsymbol{x}'$. Thus, $\varepsilon_{x'x'}$ remains constant across all tract-aligned coordinate systems and was expressed by equation (6).

In the current study, the peak values of equations 9-13 across the range of θ_i were considered. The analytical solutions for the peak values for the 5 strain components as well as peak conditions are summarized in Table 1. Since the peak values of $\varepsilon_{y_i'y_i'}(\theta_i)$ and $\varepsilon_{z_i'z_i'}(\theta_i)$ are identical, these two variables were combined as one and further referred to as tract-vertical strain (Fig. 2E) [52], measuring the normal deformation vertical (or perpendicular) to fiber tracts. Similarly, the peak values of $\varepsilon_{x'y_i'}(\theta_i)$ and $\varepsilon_{x'z_i'}(\theta_i)$ were combined as one variable and further referred to as axial shear

strain (Fig. 2E) [51], quantifying shear deformation along the fiber tracts. The peak value of $\varepsilon_{y_i' z_i'}(\theta_i)$ was termed lateral-shear strain (Fig. 2E) [52], describing the shear deformation vertical to the fiber tracts. Consequently, once the strain tensor and real-time fiber orientation are known, the four tract-related strains can be calculated directly using the analytically derived formulas (Table 1).

Table 1. Analytical formulas for the tract-related strains described by equation 6 and equation 9-13, and the corresponding conditions attaining the peak values.

Strain	Symbol	Peak value	Peak condition
Tract-oriented strain	$\varepsilon_{x'x'}$	$\boldsymbol{v}^T \cdot \boldsymbol{E}_{\text{skull}} \cdot \boldsymbol{v}$	Constant across all tract-aligned coordinate systems
Tract-vertical strain	$\varepsilon_{y_i' y_i'}(\theta_i)$	$\frac{\varepsilon_{y_1' y_1'} + \varepsilon_{z_1' z_1'}}{2} + \sqrt{(\frac{\varepsilon_{y_1' y_1'} - \varepsilon_{z_1' z_1'}}{2})^2 + \varepsilon_{y_1' z_1'}^2}$	$\sin(2\theta_i + \phi_1) = -1$
	$\varepsilon_{z_i' z_i'}(\theta_i)$	$\frac{\varepsilon_{y_1' y_1'} + \varepsilon_{z_1' z_1'}}{2} + \sqrt{(\frac{\varepsilon_{y_1' y_1'} - \varepsilon_{z_1' z_1'}}{2})^2 + \varepsilon_{y_1' z_1'}^2}$	$\sin(2\theta_i + \phi_2) = 1$
Axial-shear strain	$\varepsilon_{x' y_i'}(\theta_i)$	$\sqrt{\varepsilon_{x' y_1'}^2 + \varepsilon_{x' z_1'}^2}$	$\sin(\theta_i + \phi_3) = -1$
	$\varepsilon_{x' z_i'}(\theta_i)$	$\sqrt{\varepsilon_{x' y_1'}^2 + \varepsilon_{x' z_1'}^2}$	$\sin(\theta_i + \phi_4) = 1$
Lateral-shear strain	$\varepsilon_{y_i' z_i'}(\theta_i)$	$\sqrt{(\frac{\varepsilon_{y_1' y_1'} - \varepsilon_{z_1' z_1'}}{2})^2 + \varepsilon_{y_1' z_1'}^2}$	$\sin(2\theta_i + \phi_5) = 1$

The derivation described above was extended to all timesteps and all WM elements towards a comprehensive description of the WM tract-related deformations compared to previous studies where only the tract-oriented strain was presented [9, 25, 29-32, 36-45, 47-50, 62-64]. This derivation assumed that the displacements across the fiber tracts and surrounding matrix were continuous. The yielded analytical solutions are consistent with previous results in the *in vitro* models for special cases of simple shear [52, 53] and compression [51].

Loading condition

Simulations of clinically diagnosed head impacts were conducted, through which strain-based measures were obtained. At Stanford University, instrumented mouthguards have been developed to measure six-degree-of-freedom head kinematics during in-game head impacts in athletes [65, 66]. Using these instrumented mouthguards, over 500 head impacts in football have been tracked and video-confirmed [67]. In the current study, two concussed impacts (i.e., one with

the athlete suffering alteration of consciousness, and the other with the player had a milder but self-reported concussion) and 113 randomly-selected non-concussed impacts were simulated [67]. Each impact trace possessed a recorded duration of 100 ms.

To further enrich the loading cases, 53 football impacts in a recently analyzed database of National Football League (NFL) collisions [68] were simulated. The impact kinematics of these NFL collisions were obtained from laboratory reconstruction using Hybrid III anthropometric test dummies [69, 70]. While the loading traces of these 53 simulated cases exhibited varying durations ranging from 34 ms to 100 ms, a case-by-case scrutinization was performed following the requirement that the maximum strains be attained within the available impact durations. Only 36 impacts, including 15 concussive impacts and 21 non-concussive impacts, met the requirement and were retained for further analysis.

Table 2. Summary of kinematic magnitudes expressed in mean and standard deviation values of two datasets. Note the X, Y, and Z axes are the same as those in the skull-fixed coordinate system in Fig. 2B.

Reference	Impact cases (concussed)	Peak magnitudes of translation acceleration (g)			Peak magnitudes of rotational velocity (rad/s)		
		X	Y	Z	X	Y	Z
Hernandez et al. [67]	115 (2)	22.0 ± 17.7	18.1 ± 15.3	21.2 ± 24.5	9.1 ± 6.4	12.2 ± 7.4	7.9 ± 5.6
Sanchez et al. [68]	36 (15)	35.5 ± 20.2	54.4 ± 34.3	29.0 ± 14.3	24.3 ± 12.4	12.5 ± 6.8	16.3 ± 13.4
Total	151 (17)	25.2 ± 19.1	26.7 ± 26.3	23.0 ± 22.7	12.7 ± 10.5	12.3 ± 7.2	9.9 ± 8.8

In summary, a total of 151 impacts (including 17 concussed impacts and 134 non-concussed impacts) were considered from the two datasets (Table 2). In each simulation, the skull was assumed to be rigid, and the translational and rotational accelerations were prescribed to a node located at the center of gravity of the FE head model and rigidly attached to the skull. A selectively reduced integration scheme was used for all the brain components and CSF. A typical simulation of 90 ms required about 11 hours using LS-DYNA 11.0 with double precision on a local Linux cluster with a single processor. The model responses were output at every 0.5 ms.

Strain-based injury metrics

The injury predictability of the 4 tract-related strain peaks (i.e., maximum tract-oriented strain (MTOS), maximum tract-vertical strain (MTVS), maximum axial-shear strain (MASS), and maximum lateral-shear strain (MLSS)) and the MPS were evaluated (Table 3). For these five strain-

based metrics, the 95th percentile maximum values in five commonly injured sub-regions (i.e., cerebral WM, brainstem, midbrain, corpus callosum, and thalamus) and the whole WM were obtained. Note that the injury predictability of these 5 strain-based metrics was evaluated at the regional level, similar to previous studies [22, 38, 47, 71].

Table 3. Summary of the abbreviation of the metrics evaluated in this study and the corresponding description.

Abbreviation	Description
MPS	The peak of the 1st principal Green-Lagrange strain across the entire simulation.
MTOS	The peak of normal strain along the white matter fiber tracts across the entire simulation.
MTVS	The peak of normal strain vertical (perpendicular) to the white matter fiber tracts across the entire simulation.
MASS	The peak of shear strain along the white matter fiber tracts across the entire simulation.
MLSS	The peak of shear strain vertical (perpendicular) to the white matter fiber tracts across the entire simulation.

Statistical analysis

While the four tract-related strains are fundamentally different measures according to their analytical formulas in Table 1, the interdependence between the MPS and four tract-related strain metrics remained unclear. To ascertain this, we conducted a one-way repeated measures analysis of variance (ANOVA) test between MPS and each of four tract-related strains, respectively. The tests were performed based on the element-wise peak values across the entire simulation for all WM elements (N=1323) from the simulation of a representative concussive impact (i.e., Case 157H2 from the NFL dataset).

We next evaluated the injury predictability of 5 strain-based metrics (Table 3) in terms of discriminating the concussive and non-concussive cases. To correlate the binary injury outcome (i.e., concussion or non-concussion) with the continuous injury metrics in 6 regions of interest (ROI), survival analysis with a Weibull distribution was employed (N=151). The survival analysis treats all data as double censored, producing a model that is more appealing on physical groups, while a Weibull distribution always satisfies a zero risk of injury for zero force. This statistical model was similarly adopted in previous biomechanical studies [41, 50] with the detailed merits available in [72].

To further assure an objective comparison and maximize the training dataset, all survival analyses were conducted within a leave-one-out cross-validation (LOOCV) framework [63, 64]. To evaluate the sensitivity and specificity of each strain-based metric to separate the concussion and non-concussive cases, the receiver operating characteristic (ROC) curve analysis was generated both for the testing and training datasets based on a threshold of 50% injury probability. The area under each ROC curve (AUC) was calculated with a higher value indicating better injury predictability and a value of 0.5 for a random guess.

All the statistical analyses were performed with custom scripts in MATLAB (R2016b, MathWorks, Natick, MA) with built-in statistical toolbox functions and SPSS (22.0, SPSS Inc. Chicago, Illinois). The threshold for significance was $p<0.05$.

Results

Case illustration

To demonstrate the applicability of the proposed analytical formulas in Table 1 to computing the tract-related strains, we employed Case 157H2 from the NFL dataset as a representative impact for illustration purposes. Case 157H2 is a concussive impact in which the football player was laterally struck, resulting in high angular velocities in the coronal and sagittal planes. The impact duration was 50 ms.

Computation of tract-related strains for one element

As exemplified by one randomly selected element in the corpus callosum in Fig. 3, the first principal strain was directly output from the LS-DYNA solver for each timestep. To acquire the tract-related strains, both the strain tensor of the exemplified element and the temporal orientation of the embedded truss element were extracted from the pre-computed simulation and then transformed within the skull-fixed coordinate system. Hence, four strain-based measures pertaining to the fiber tracts were computed using the analytical formulas in Table 1. The peaks of these four tract-related

strain measures plus the maximum principle strain over the entire simulation were considered as potential injury metrics in the current study. For this specific element, the value (occurring time) of each metric is highlighted in Fig. 3.

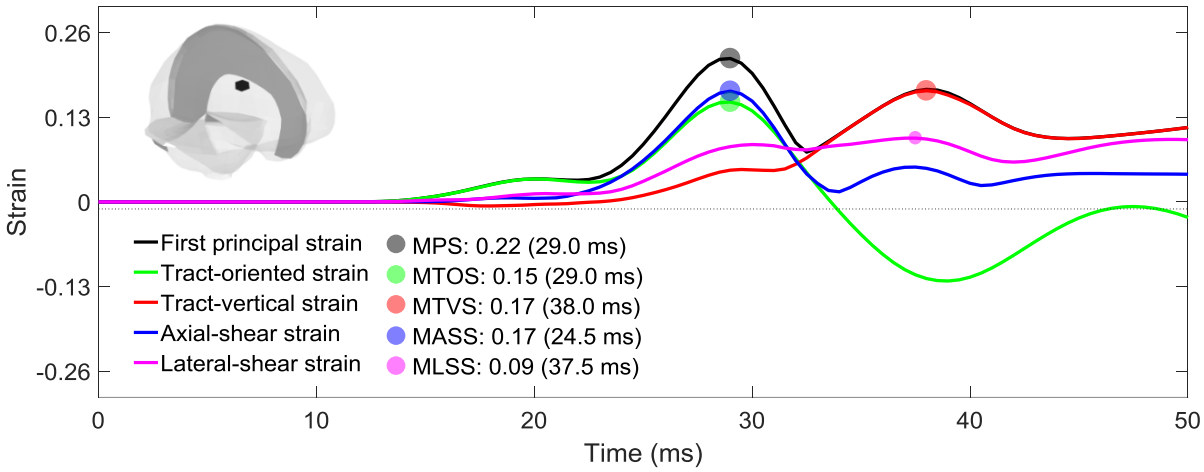

Fig. 3. Time history curves of strain-based measures for one representative element in the corpus callosum (highlighted in black within the whole-brain thumbnail in the top-left corner) during a simulation of a concussed impact (Case 157H2). The peak values for all curves were highlighted as filled dots that were considered as injury metrics in the current study.

Computation of tract-related strains for one impact

The calculation detailed above for one representative element was applied to all WM elements in the FE model for the illustrated case. The WM elements with the values of each metric above 0.13, a conservative threshold proposed by Bain and Meaney [73] that instigated electrophysiological impairment to the optic nerve of an adult male guinea pig under dynamic stretching, were identified (Fig. 4A-B). Distinct differences were noted among the five metrics in terms of volume fraction and spatial distribution of WM regions with high strains. The WM volume fractions identified by this electrophysiological threshold were 0.76 for MPS, 0.41 for MTVS, 0.29 for MASS, 0.20 for MLSS, and 0.19 for MTOS. Comparable differences were also noted when extending the WM volume fraction as a function of the strain thresholds (Fig. 4B).

To evaluate the interdependence between MPS and its tract-related counterparts, a one-way repeated measures ANOVA test was conducted between MPS and each of the four tract-related metrics, respectively, based on the results of all WM elements (N=1323). A p-value less than 0.001

was attained for all four tests, indicating the lack of interdependence between MPS and the tract-related metrics (Fig. 4C).

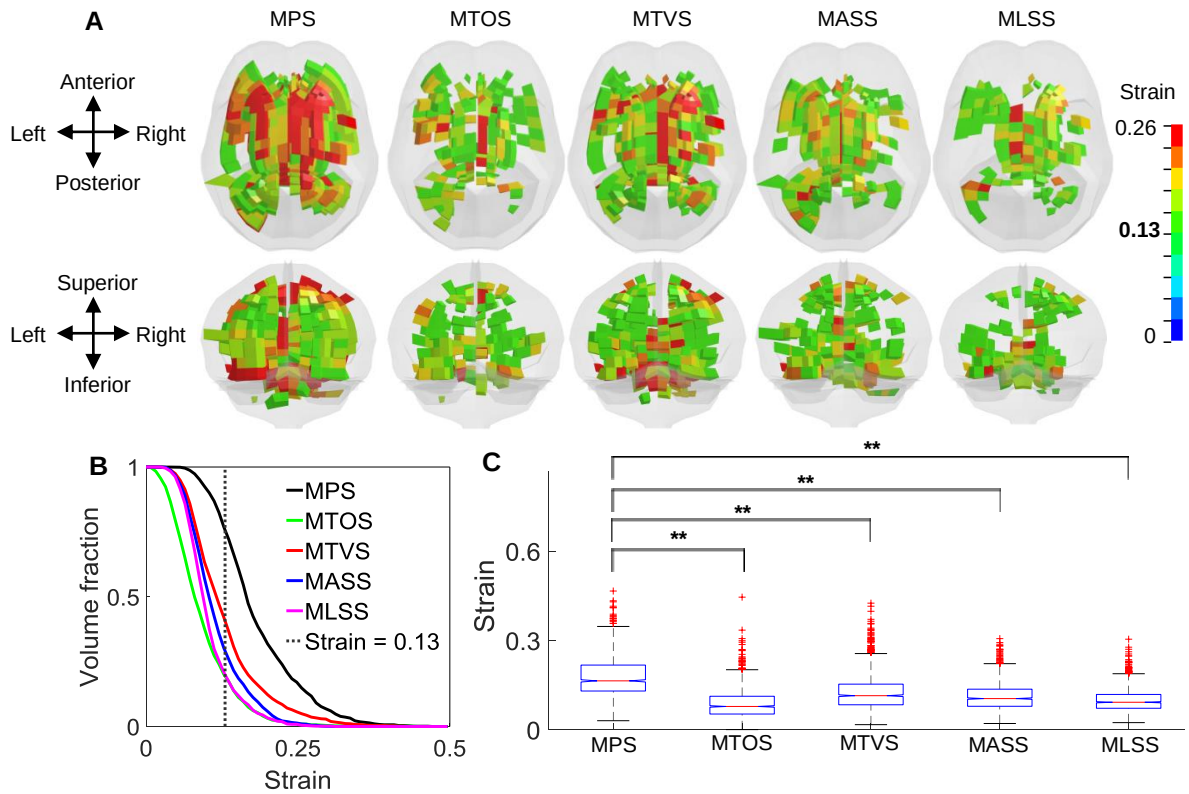

Fig. 4. Model-estimated results based on 5 strain-based metrics in a representative impact involving one striking player with a concussion (Case 157H2) showing independence of the metrics. (A) Axial and coronal view of white matter elements with strain peaks over 0.13 (i.e., a conservative electrophysiological impairment threshold proposed by Bain and Meaney [73] identified by 5 strain-based metrics. (B) Volume fraction of WM elements with peak strains above different strain levels (a threshold of 0.13 shown as a dotted line). (C) Element-wise strain-based metrics for all white matter elements (N = 1323). Statistical difference in one-way repeated measures ANOVA test between MPS and each of four tract-related strains are reported as ** when p<0.001. On each box, the central line (red) is the median value, and the upper and lower edges (blue) of the box are the 25th and 75th percentile values, while the ±2.7*standard deviation from the mean is shown as horizontal lines (black) and the outliers are shown as '+' symbol (red).

Injury predictability of strain-based metrics

We next evaluated the discrimination performance of 5 strain-based metrics in terms of separating the concussive and non-concussive cases. A summary of the model-estimated metrics for different ROIs is presented in Fig. 5. The mean values and standard deviations observed in the simulations are illustrated for concussed and un-concussed players in the cerebral WM, brainstem, midbrain, corpus callosum, thalamus, and whole WM. A statistical difference (t-test, p<0.01) between concussed and un-concussed players was attained for all 5 metrics across all 6 ROIs.

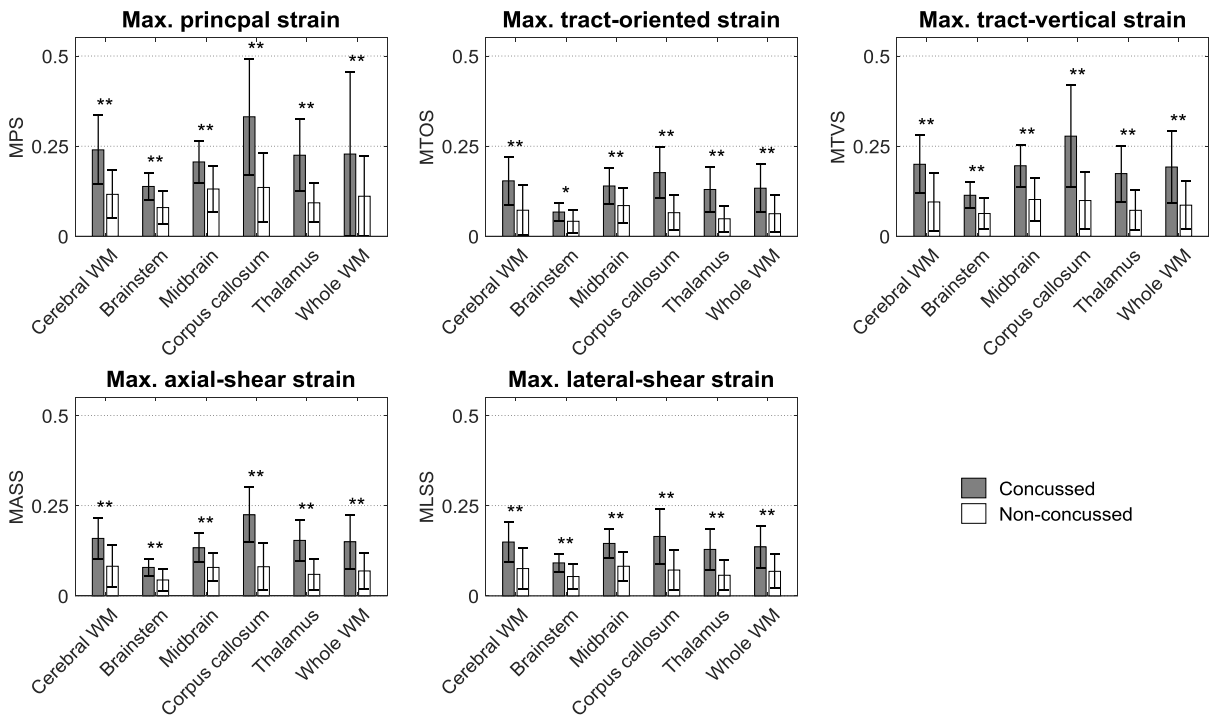

Fig. 5. A summary of the mean values and standard deviations of regional 95th percentile strain-based metrics. The values are shown in black for concussed (n=17) and white for non-injured (n=134) players for various anatomical regions and whole white matter in the brain model. Statistical differences in t-tests are reported (*p<0.01; **p<0.001).

The injury predictability of the five strain-based metrics in discriminating concussed from non-concussed cases was evaluated via survival analysis with the performance quantified by AUC values within a LOOCV framework. Fig. 6 shows the ROC curves for different strain-based metrics in different ROIs for the testing dataset. The AUC values for all metrics in all ROIs were over 0.5 (the AUC for a random guess). For the five strain-based metrics, the AUC values of all four tract-related metrics were consistently larger than that of MPS across all ROIs, while the metrics with the highest AUC values were region-dependent. For the cerebral WM, the MLSS exhibited the highest AUC value as 0.874, while MASS for brainstem (AUC = 0.868), MTVS for midbrain (AUC = 0.867), MTOS for corpus callosum (AUC = 0.909) and thalamus (AUC = 0.901), and MTVS for whole WM (AUC = 0.869). Similar findings were revealed by the training dataset with detailed results in Fig. A1 in Appendix.

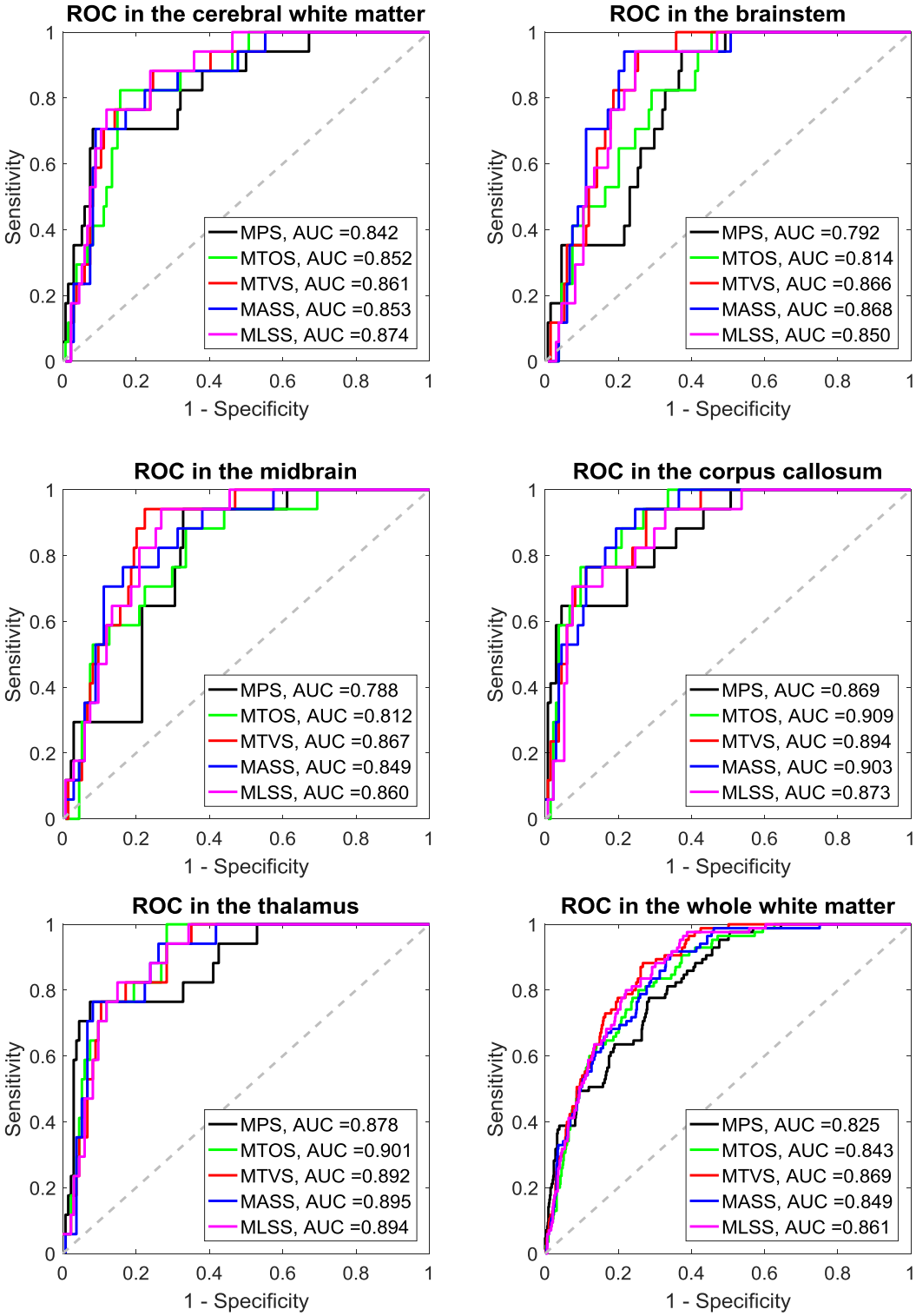

Fig. 6. Receiver operator curve (ROC) for the 5 strain-based metrics in different regions of the brain based on the testing dataset within the leave-one-out cross-validation framework. The area under the curve is also reported for each metric. In each subfigure, the 50% probability line (gray dash) indicates the level of a random guess (i.e., AUC=0.5).

Discussions

The current study detailed a theoretical strain analysis to comprehensively quantify the deformation of the WM fiber tracts through coordinate transformations, in which the strain tensor of each WM element was transformed to the coordinate systems with one axis aligned with the real-time fiber orientation. Three novel tract-related strains were extracted, characterizing the normal deformation vertical to the fiber tracts, and shear deformation along and vertical to the fiber tracts, respectively. The injury predictability of these three newly-proposed strain peaks was evaluated by correlating these metrics with injury outcome and compared to that of the previously-used MTOS and MPS. It was verified that four tract-related strain peaks exhibited superior performance in discriminating the concussion and non-concussion cases than the MPS. This comprehensive delineation of the deformation pertaining to the WM fiber tracts suggests the preferential use of tract-related strains as predictors for brain injury.

When focusing on MPS and MTOS, enhanced performance on injury discrimination was noted for MTOS with respect to MPS, correlating well with the findings in previous computational studies [25, 38, 40, 41, 47, 74]. However, possibly because of the lack of consensus of brain mechanics, substantial differences existed among the previous studies, particularly on the brain materials (e.g., isotropic vs. anisotropic, heterogeneous vs. homogeneous) and the computation of tract-oriented strain (e.g., time-variant fiber orientation vs. time-invariant fiber orientation) [49]. The current study was unique since we simulated the brain as an isotropic and homogenous structure and leveraged an embedded element approach to monitor the real-time fiber orientation during head impacts. This orientation information was further used to inform the calculation of tract-oriented strain by projecting the strain tensors from pre-computed simulation along the real-time fiber direction. Thus, the current study can be regarded as a significant extension to previous efforts [25, 38, 40, 41, 47, 74], collectively further reinforcing the importance of adopting orientation-dependent metrics as predictors for brain injury, especially when it comes to concussion or axonal injury.

Besides the MPS and MTOS, the current study proposed three new tract-related strain peaks as injury metrics, i.e., MTVS, MASS, and MLSS, contributing to a comprehensive delineation of WM tract-related deformation with respect to the previous practice where only the MTOS was presented [9, 25, 29-45, 47-49, 74, 75]. By correlating the injury metrics with the injury outcome, the three newly-proposed metrics exhibited comparable discrimination performance to the MTOS, but were consistently superior to the MPS. These results were extensively supported by the findings in *in vivo*, *ex vivo*, and *in vitro* experimental models [51-54, 73, 76-85]. For example, LaPlaca et al. [53] found that a significant loss of neurites in the *in vitro* model occurred in the regime at which the axial-shear strain peaked. More recently, another *in vitro* model [51] also found that the spatial distribution of high axial-shear strains correlated with the localization of neurite blebbing. By imposing uniaxial stretching to a 2D culture slices with the orientation of the embedded axons quantified, Nakadate et al. [54] found swellings were concomitantly noted in these axons with their orientations parallel and perpendicular to the stretching direction, indicating that both the tract-oriented strain and tract-vertical strain might instigate axonal injury. Collectively, the congruency between the current study and experimental models further highlights the potential of the three newly-proposed tract-related strains and the previously-used tract-oriented strain as injury predictors compared to MPS. Nevertheless, it is worth clarifying that the scale of interest in the *in vivo*, *ex vivo*, and *in vitro* models (e.g., axon/neuron/nerve fiber) may not necessarily be the same as the one in our computational results (i.e., fiber tracts).

Among the four tract-related strain metrics, a regional-dependency was noted for the best injury predictor. In all regions, the AUC value of the best predictor was only marginally larger than the three others. Such results might be partially related to the binary injury outcome of the simulated impacts (i.e., concussion or non-concussion), lacking definitive documentation of localization and extent of injury pathology. This was further confounded by the fact that no definitive consensus has been reached regarding the clinical criteria for concussion diagnosis [86, 87]. Recent studies have also supported that concussion does not inform the pathological cascade secondary to

exterior insults and cannot be regarded as a true diagnosis [88]. Thus, the oversimplified injury outcome, as well as associated compounding factors, in the concussion diagnosis of the two simulated datasets [67, 68] prohibits further discrimination among these four tract-related strain metrics. In addition, the discrimination performance of all metrics was evaluated based on the 95th percentile peak strain values at 6 ROIs, the same as the strategy in previous studies [22, 38, 47, 71]. This strategy is a typical down-sampling operation, in which the spatiotemporally-detailed strain information estimated by the FE model was represented by one single variable characterizing the peaking response over time across a pre-defined region. The reliability of such a down-sampling operation and corresponding effects on injury prediction performance remains to be further investigated [47, 48]. Nevertheless, as exemplified by one representative element in Fig. 3, the fiber tracts experienced alternate combinations of normal and shear deformation with the predominant mode varied across the timespan of the impact. It might be possible that brain injury was the synergistic outcome of various strains with their effects either alternately or simultaneously exerted. Thus, one possible direction for future work could be identifying the synergism of combined strain measures and corresponding influence on injury discrimination.

Axonal injury is a complex injury with a wide spectrum of pathological severity, ranging from mild levels, which can be associated with subtle neurological deficits pertaining to electrophysiological impairment, to several forms, which can lead to a large scale of neuronal degeneration/death throughout the WM [89, 90]. Through careful spatiotemporal correlation between specific manifestation of neural pathology and various strain measures, an *in vitro* model recently found that the bleb formation was strongly correlated with axial-shear strain, while being uncorrelated with the tract-oriented strain [51]. Inversely, the timeframe of neuronal death was only correlated with the integral of tract-oriented strain over the length of the neuron, rather than its counterparts based on the axial-shear strain [51]. Such results highlighted that the four tract-related strains might have the potential of discriminating different pathological demonstrations. Thus far, the authors are not aware of such an injury dataset with definitive documentation of the location

and specific manifestation of injury pathology as well as accurate measurement of the impact loading in humans. A further evaluation of the tract-related strains on their discrimination capability of specific pathological manifestation warrants further work.

As reflected by our modeling choice that no relative motion between the truss elements and their master elements were permitted [49], these analytical solutions in Table 1 were attained based on the assumption that the displacements across the fiber tracts and surrounding matrix was continuous, similar to the assumption in the aforementioned *in vitro* models [51-53] and other computational studies [29, 30, 40, 41, 46, 74, 75, 91]. This assumption was partially verified by one *in vitro* model, in which no evident movement of soma/neurite with respect to the surrounding matrix was observed in the rat [53]. However, the authors acknowledge that a systematic examination of the coupling response between the WM fiber tracts and surrounding matrix in humans was deemed necessary.

The presented theoretical framework can also be extendedly implemented to other TBI scenarios, such as mapping strains onto the branched microstructures of the vasculature to uncover the underlying mechanical cue for the blood-brain barrier, and even far beyond the central nervous system. An extensive discussion regarding the potential implementation of the current theoretical framework can be found in [92]. Another important implication of the current work is to guide the multiscale modeling of axonal injury, that explore the mechanobiological pathway of axonal injury from the macroscopic loads endured at the whole head level to the cellular/molecular level. Current multiscale endeavors often employ a single mode of loading, such as uniaxial stretching (corresponding to the tract-oriented strain in the current study) [93-97]. Our work might better inform the multiscale modeling with diverse and combined loadings.

The orientation information of WM fiber tracts embedded within the FE head model is based on the primary eigenvector of the diffusion tensor, but there is considerable information in the MRI-derived diffusion tensor that could be synergistic with the current sophisticated modelling [98].

Furthermore, it is well-known that the tensor model is a limited approximation of the complexity of human white matter, in which many fiber bundles intertwine and cross, and other more sophisticated models exist and could be considered for future work [99]. Additional limitations (e.g., simulating the brain as an isotropic and homogeneous medium, imaging resampling operation when couple the DTI-revealed orientation with the WM element, etc.) are present and unchanged from previous work [49].

Conclusion

The present study performed a theoretical strain derivation to comprehensively quantify the deformation pertaining to the WM fiber tracts by relating the strain tensor of the WM element to its embedded fiber tract. In addition to the previously used tract-oriented strain quantifying the normal deformation along the fiber tracts, three new tract-related strains were proposed, characterizing the normal deformation vertical to the fiber tracts and shear deformation along and vertical to the fiber tracts. By relating the continuous injury criteria and binary injury outcome, it was revealed that all tract-related strain peaks demonstrate enhanced discriminating capability of separating the concussion and non-concussion cases than the MPS, advocating the further investigation of tract-related metrics as injury predictors. This study presents a comprehensive delineation of WM tract-related deformation and advocates the use of orientation-dependent criteria with injury criteria, which may ultimately contribute to an advanced mechanobiological understanding and enhanced computational predictability of axonal injury.

Conflict of Interest

Drs. Michael Zeineh, Gerald Grant, and David Camarillo received funding from the Pac-12 Conference's Student-Athlete Health and Well-Being Initiative and Taube Stanford Children's Concussion Initiative. Drs. Svein Kleiven and Xiaogai Li received funding from the Swedish Research Council (VR-2016-05314 and VR-2016-04203), while Dr. Marios Georgiadis received funding from the Swiss National Science Foundation (P400PM_180773). The content of this article is solely the

responsibility of the authors and does not necessarily represent the official views of funding agencies. The simulations were performed on resources provided by the Swedish National Infrastructure for Computing (SNIC) at the center for High Performance Computing (PDC). The authors also thank Dr. Annaclaudia Montanino for the valuable sharing of literature knowledge.

References

[1] C.A. Taylor, J.M. Bell, M.J. Breiding, L. Xu, Traumatic brain injury–related emergency department visits, hospitalizations, and deaths—United States, 2007 and 2013, MMWR Surveillance Summaries, 66 (2017) 1.
[2] W. Peeters, R. van den Brande, S. Polinder, A. Brazinova, E.W. Steyerberg, H.F. Lingsma, A.I. Maas, Epidemiology of traumatic brain injury in Europe, Acta neurochirurgica, 157 (2015) 1683-1696.
[3] J. Olesen, A. Gustavsson, M. Svensson, H.U. Wittchen, B. Jönsson, C.S. Group, E.B. Council, The economic cost of brain disorders in Europe, European journal of neurology, 19 (2012) 155-162.
[4] B. Roozenbeek, A.I. Maas, D.K. Menon, Changing patterns in the epidemiology of traumatic brain injury, Nature Reviews Neurology, 9 (2013) 231.
[5] V.E. Johnson, W. Stewart, M.T. Weber, D.K. Cullen, R. Siman, D.H. Smith, SNTF immunostaining reveals previously undetected axonal pathology in traumatic brain injury, Acta neuropathologica, 131 (2016) 115-135.
[6] P.P. Tsitsopoulos, S. Abu Hamdeh, N. Marklund, Current opportunities for clinical monitoring of axonal pathology in traumatic brain injury, Frontiers in neurology, 8 (2017) 599.
[7] V.E. Johnson, W. Stewart, D.H. Smith, Axonal pathology in traumatic brain injury, Experimental neurology, 246 (2013) 35-43.
[8] A. Goriely, M.G. Geers, G.A. Holzapfel, J. Jayamohan, A. Jérusalem, S. Sivaloganathan, W. Squier, J.A. van Dommelen, S. Waters, E. Kuhl, Mechanics of the brain: perspectives, challenges, and opportunities, Biomechanics and modeling in mechanobiology, 14 (2015) 931-965.
[9] X. Li, Z. Zhou, S. Kleiven, An anatomically detailed and personalizable head injury model: Significance of brain and white matter tract morphological variability on strain, Biomechanics and modeling in mechanobiology, (2020) 1-29.
[10] Z. Zhou, X. Li, S. Kleiven, W.N. Hardy, Brain strain from motion of sparse markers, SAE Technical Paper, 2020.
[11] X. Li, H. Sandler, S. Kleiven, Infant skull fractures: Accident or abuse?: Evidences from biomechanical analysis using finite element head models, Forensic science international, 294 (2019) 173-182.
[12] X. Li, H. Sandler, S. Kleiven, The importance of nonlinear tissue modelling in finite element simulations of infant head impacts, Biomechanics and modeling in mechanobiology, 16 (2017) 823-840.
[13] L.A. Mihai, S. Budday, G.A. Holzapfel, E. Kuhl, A. Goriely, A family of hyperelastic models for human brain tissue, Journal of the Mechanics and Physics of Solids, 106 (2017) 60-79.
[14] S. Budday, G. Sommer, C. Birkl, C. Langkammer, J. Haybaeck, J. Kohnert, M. Bauer, F. Paulsen, P. Steinmann, E. Kuhl, Mechanical characterization of human brain tissue, Acta biomaterialia, 48 (2017) 319-340.
[15] Z. Zhou, X. Li, S. Kleiven, Evaluation of brain-skull interface modelling approaches on the prediction of acute subdural hematoma in the elderly, Journal of biomechanics, 105 (2020) 109787.
[16] H. Duckworth, D.J. Sharp, M. Ghajari, Smoothed Particle Hydrodynamic Modelling of the Cerebrospinal Fluid for Brain Biomechanics: Accuracy and Stability, International Journal for Numerical Methods in Biomedical Engineering, (2021).

[17] Z. Zhou, X. Li, S. Kleiven, Biomechanics of periventricular injury, Journal of neurotrauma, 37 (2020) 1074-1090.
[18] Z. Zhou, B. Jiang, L. Cao, F. Zhu, H. Mao, K.H. Yang, Numerical simulations of the 10-year-old head response in drop impacts and compression tests, computer methods and programs in biomedicine, 131 (2016) 13-25.
[19] D. Marjoux, D. Baumgartner, C. Deck, R. Willinger, Head injury prediction capability of the HIC, HIP, SIMon and ULP criteria, Accident Analysis & Prevention, 40 (2008) 1135-1148.
[20] E. O'Keeffe, E. Kelly, Y. Liu, C. Giordano, E. Wallace, M. Hynes, S. Tiernan, A. Meagher, C. Greene, S. Hughes, Dynamic blood–brain barrier regulation in mild traumatic brain injury, Journal of neurotrauma, 37 (2020) 347-356.
[21] J. Ho, Z. Zhou, X. Li, S. Kleiven, The peculiar properties of the falx and tentorium in brain injury biomechanics, Journal of biomechanics, 60 (2017) 243-247.
[22] S. Kleiven, Predictors for Traumatic Brain Injuries Evaluated Through Accident Reconstructions, Stapp car crash journal, 51 (2007) 81-114.
[23] Z. Zhou, X. Li, S. Kleiven, W.N. Hardy, Brain Strain From Motion of Sparse Markers, Stapp car crash journal, 63 (2019) 1-27.
[24] M. Ghajari, P.J. Hellyer, D.J. Sharp, Computational modelling of traumatic brain injury predicts the location of chronic traumatic encephalopathy pathology, Brain, 140 (2017) 333-343.
[25] S. Sullivan, S.A. Eucker, D. Gabrieli, C. Bradfield, B. Coats, M.R. Maltese, J. Lee, C. Smith, S.S. Margulies, White matter tract-oriented deformation predicts traumatic axonal brain injury and reveals rotational direction-specific vulnerabilities, Biomechanics and modeling in mechanobiology, 14 (2015) 877-896.
[26] E.G. Takhounts, S.A. Ridella, V. Hasija, R.E. Tannous, J.Q. Campbell, D. Malone, K. Danelson, J. Stitzel, S. Rowson, S. Duma, Investigation of Traumatic Brain Injuries Using the Next Generation of Simulated Injury Monitor (SIMon) Finite Element Head Model, Stapp car crash journal, 52 (2008) 1-31.
[27] S. Mori, K. Oishi, H. Jiang, L. Jiang, X. Li, K. Akhter, K. Hua, A.V. Faria, A. Mahmood, R. Woods, Stereotaxic white matter atlas based on diffusion tensor imaging in an ICBM template, Neuroimage, 40 (2008) 570-582.
[28] S. Mori, J. Zhang, Principles of diffusion tensor imaging and its applications to basic neuroscience research, Neuron, 51 (2006) 527-539.
[29] H.T. Garimella, R.H. Kraft, Modeling the mechanics of axonal fiber tracts using the embedded finite element method, International journal for numerical methods in biomedical engineering, 33 (2017) e2823.
[30] T. Wu, A. Alshareef, J.S. Giudice, M.B. Panzer, Explicit modeling of white matter axonal fiber tracts in a finite element brain model, Annals of biomedical engineering, 47 (2019) 1908-1922.
[31] W. Zhao, J.C. Ford, L.A. Flashman, T.W. McAllister, S. Ji, White matter injury susceptibility via fiber strain evaluation using whole-brain tractography, Journal of neurotrauma, 33 (2016) 1834-1847.
[32] S. Chatelin, C. Deck, F. Renard, S. Kremer, C. Heinrich, J.-P. Armspach, R. Willinger, Computation of axonal elongation in head trauma finite element simulation, Journal of the mechanical behavior of biomedical materials, 4 (2011) 1905-1919.
[33] R. Cloots, J. Van Dommelen, M. Geers, A tissue-level anisotropic criterion for brain injury based on microstructural axonal deformation, Journal of the mechanical behavior of biomedical materials, 5 (2012) 41-52.
[34] R. Cloots, J. Van Dommelen, T. Nyberg, S. Kleiven, M. Geers, Micromechanics of diffuse axonal injury: influence of axonal orientation and anisotropy, Biomechanics and modeling in mechanobiology, 10 (2011) 413-422.
[35] R.J. Cloots, J. Van Dommelen, S. Kleiven, M. Geers, Multi-scale mechanics of traumatic brain injury: predicting axonal strains from head loads, Biomechanics and modeling in mechanobiology, 12 (2013) 137-150.

[36] S. Ganpule, N.P. Daphalapurkar, K.T. Ramesh, A.K. Knutsen, D.L. Pham, P.V. Bayly, J.L. Prince, A three-dimensional computational human head model that captures live human brain dynamics, Journal of neurotrauma, 34 (2017) 2154-2166.
[37] C. Giordano, R. Cloots, J. Van Dommelen, S. Kleiven, The influence of anisotropy on brain injury prediction, Journal of biomechanics, 47 (2014) 1052-1059.
[38] C. Giordano, S. Kleiven, Evaluation of Axonal Strain as a Predictor for Mild Traumatic Brain Injuries Using Finite Element Modeling, Stapp Car Crash Journal, 58 (2014) 29-61.
[39] C. Giordano, S. Zappalà, S. Kleiven, Anisotropic finite element models for brain injury prediction: the sensitivity of axonal strain to white matter tract inter-subject variability, Biomechanics and modeling in mechanobiology, 16 (2017) 1269-1293.
[40] M. Hajiaghamemar, S.S. Margulies, Multi-scale white matter tract embedded brain finite element model predicts the location of traumatic diffuse axonal injury, Journal of Neurotrauma, 38 (2021) 144-157.
[41] M. Hajiaghamemar, T. Wu, M.B. Panzer, S.S. Margulies, Embedded axonal fiber tracts improve finite element model predictions of traumatic brain injury, Biomechanics and modeling in mechanobiology, (2019) 1-22.
[42] F. Hernandez, C. Giordano, M. Goubran, S. Parivash, G. Grant, M. Zeineh, D. Camarillo, Lateral impacts correlate with falx cerebri displacement and corpus callosum trauma in sports-related concussions, Biomechanics and modeling in mechanobiology, 18 (2019) 631-649.
[43] S. Ji, W. Zhao, J.C. Ford, J.G. Beckwith, R.P. Bolander, R.M. Greenwald, L.A. Flashman, K.D. Paulsen, T.W. McAllister, Group-wise evaluation and comparison of white matter fiber strain and maximum principal strain in sports-related concussion, Journal of neurotrauma, 32 (2015) 441-454.
[44] R.M. Wright, A. Post, B. Hoshizaki, K.T. Ramesh, A multiscale computational approach to estimating axonal damage under inertial loading of the head, Journal of neurotrauma, 30 (2013) 102-118.
[45] R.M. Wright, K. Ramesh, An axonal strain injury criterion for traumatic brain injury, Biomechanics and modeling in mechanobiology, 11 (2012) 245-260.
[46] T. Wu, J. Antona-Makoshi, A. Alshareef, J.S. Giudice, M.B. Panzer, Investigation of cross-species scaling methods for traumatic brain injury using finite element analysis, Journal of neurotrauma, 37 (2020) 410-422.
[47] W. Zhao, Y. Cai, Z. Li, S. Ji, Injury prediction and vulnerability assessment using strain and susceptibility measures of the deep white matter, Biomechanics and modeling in mechanobiology, 16 (2017) 1709-1727.
[48] W. Zhao, S. Ji, White matter anisotropy for impact simulation and response sampling in traumatic brain injury, Journal of neurotrauma, 36 (2019) 250-263.
[49] Z. Zhou, A.G. Domel, X. Li, G. Grant, S. Kleiven, D.B. Camarillo, M. Zeineh, White matter tract-oriented deformation is dependent on real-time axonal fiber orientation, Journal of neurotrauma, (2021).
[50] T. Wu, M. Hajiaghamemar, J.S. Giudice, A. Alshareef, S. Margulies, M.B. Panzer, Evaluation of Tissue-Level Brain Injury Metrics Using Species-Specific Simulations, Journal of Neurotrauma, (2021).
[51] E. Bar-Kochba, M.T. Scimone, J.B. Estrada, C. Franck, Strain and rate-dependent neuronal injury in a 3D in vitro compression model of traumatic brain injury, Scientific Reports, 6 (2016) 1-11.
[52] D.K. Cullen, M.C. LaPlaca, Neuronal response to high rate shear deformation depends on heterogeneity of the local strain field, Journal of neurotrauma, 23 (2006) 1304-1319.
[53] M.C. LaPlaca, D.K. Cullen, J.J. McLoughlin, R.S. Cargill II, High rate shear strain of three-dimensional neural cell cultures: a new in vitro traumatic brain injury model, Journal of biomechanics, 38 (2005) 1093-1105.
[54] H. Nakadate, E. Kurtoglu, H. Furukawa, S. Oikawa, S. Aomura, A. Kakuta, Y. Matsui, Strain-rate dependency of axonal tolerance for uniaxial stretching, Stapp car crash journal, 61 (2017) 53-65.
[55] S. Kleiven, W.N. Hardy, Correlation of an FE Model of the Human Head with Local Brain Motion: Consequences for Injury Prediction, Stapp Car Crash journal, 46 (2002) 123-144.

[56] Z. Zhou, X. Li, S. Kleiven, Fluid–structure interaction simulation of the brain–skull interface for acute subdural haematoma prediction, Biomechanics and modeling in mechanobiology, 18 (2019) 155-173.
[57] S. Kleiven, Evaluation of head injury criteria using a finite element model validated against experiments on localized brain motion, intracerebral acceleration, and intracranial pressure, International Journal of Crashworthiness, 11 (2006) 65-79.
[58] Z. Zhou, X. Li, S. Kleiven, C.S. Shah, W.N. Hardy, A Reanalysis of Experimental Brain Strain Data: Implication for Finite Element Head Model Validation, Stapp Car Crash Journal, 62 (2018) 293-318.
[59] S. Budday, T.C. Ovaert, G.A. Holzapfel, P. Steinmann, E. Kuhl, Fifty shades of brain: a review on the mechanical testing and modeling of brain tissue, Archives of Computational Methods in Engineering, (2019) 1-44.
[60] D.B. MacManus, B. Pierrat, J.G. Murphy, M.D. Gilchrist, Region and species dependent mechanical properties of adolescent and young adult brain tissue, Scientific reports, 7 (2017) 1-12.
[61] G.A. Holzapfel, Nonlinear solid mechanics: a continuum approach for engineering, Wiley, Chichester, UK, 2000.
[62] C. Giordano, S. Kleiven, Connecting fractional anisotropy from medical images with mechanical anisotropy of a hyperviscoelastic fibre-reinforced constitutive model for brain tissue, Journal of the Royal Society Interface, 11 (2014) 20130914.
[63] Y. Cai, S. Wu, W. Zhao, Z. Li, Z. Wu, S. Ji, Concussion classification via deep learning using whole-brain white matter fiber strains, PloS one, 13 (2018) e0197992.
[64] E.D. Anderson, J.S. Giudice, T. Wu, M.B. Panzer, D.F. Meaney, Predicting concussion outcome by integrating finite element modeling and network analysis, Frontiers in bioengineering and biotechnology, 8 (2020) 309.
[65] D.B. Camarillo, P.B. Shull, J. Mattson, R. Shultz, D. Garza, An instrumented mouthguard for measuring linear and angular head impact kinematics in American football, Annals of biomedical engineering, 41 (2013) 1939-1949.
[66] Y. Liu, A.G. Domel, S.A. Yousefsani, J. Kondic, G. Grant, M. Zeineh, D.B. Camarillo, Validation and comparison of instrumented mouthguards for measuring head kinematics and assessing brain deformation in football impacts, Annals of Biomedical Engineering, 48 (2020) 2580-2598.
[67] F. Hernandez, L.C. Wu, M.C. Yip, K. Laksari, A.R. Hoffman, J.R. Lopez, G.A. Grant, S. Kleiven, D.B. Camarillo, Six degree-of-freedom measurements of human mild traumatic brain injury, Annals of biomedical engineering, 43 (2015) 1918-1934.
[68] E.J. Sanchez, L.F. Gabler, A.B. Good, J.R. Funk, J.R. Crandall, M.B. Panzer, A reanalysis of football impact reconstructions for head kinematics and finite element modeling, Clinical biomechanics, 64 (2019) 82-89.
[69] E.J. Pellman, D.C. Viano, A.M. Tucker, I.R. Casson, Concussion in professional football: Location and direction of helmet impacts—Part 2, Neurosurgery, 53 (2003) 1328-1341.
[70] J. Newman, N. Shewchenko, E. Welbourne, A Proposed New Biomechanical Head Injury Assessment Function-The Maximum Power Index, Stapp car crash journal, 44 (2000) 215-247.
[71] L. Zhang, K.H. Yang, A.I. King, A proposed injury threshold for mild traumatic brain injury, J. Biomech. Eng., 126 (2004) 226-236.
[72] T.L. McMurry, G.S. Poplin, Statistical considerations in the development of injury risk functions, Traffic injury prevention, 16 (2015) 618-626.
[73] A.C. Bain, D.F. Meaney, Tissue-level thresholds for axonal damage in an experimental model of central nervous system white matter injury, Journal of biomechanical engineering, 122 (2000) 615-622.
[74] T. Wu, M. Hajiaghamemar, J.S. Giudice, A. Alshareef, S. Margulies, M.B. Panzer, Evaluation of Tissue-Level Brain Injury Metrics Using Species-Specific Simulations, Journal of Neurotrauma.
[75] H.T. Garimella, R.R. Menghani, J.I. Gerber, S. Sridhar, R.H. Kraft, Embedded finite elements for modeling axonal injury, Annals of biomedical engineering, 47 (2019) 1889-1907.

[76] A.C. Bain, R. Raghupathi, D.F. Meaney, Dynamic stretch correlates to both morphological abnormalities and electrophysiological impairment in a model of traumatic axonal injury, Journal of neurotrauma, 18 (2001) 499-511.
[77] D.K. Cullen, V.N. Vernekar, M.C. LaPlaca, Trauma-induced plasmalemma disruptions in three-dimensional neural cultures are dependent on strain modality and rate, Journal of neurotrauma, 28 (2011) 2219-2233.
[78] J. Galbraith, L. Thibault, D. Matteson, Mechanical and electrical responses of the squid giant axon to simple elongation, (1993).
[79] M.H. Magdesian, F.S. Sanchez, M. Lopez, P. Thostrup, N. Durisic, W. Belkaid, D. Liazoghli, P. Grütter, D.R. Colman, Atomic force microscopy reveals important differences in axonal resistance to injury, Biophysical journal, 103 (2012) 405-414.
[80] R. Shi, J. Pryor, Pathological changes of isolated spinal cord axons in response to mechanical stretch, Neuroscience, 110 (2002) 765-777.
[81] R. Shi, J. Whitebone, Conduction deficits and membrane disruption of spinal cord axons as a function of magnitude and rate of strain, Journal of neurophysiology, 95 (2006) 3384-3390.
[82] A. Singh, S. Kallakuri, C. Chen, J.M. Cavanaugh, Structural and functional changes in nerve roots due to tension at various strains and strain rates: an in-vivo study, Journal of neurotrauma, 26 (2009) 627-640.
[83] A. Singh, Y. Lu, C. Chen, S. Kallakuri, J.M. Cavanaugh, A new model of traumatic axonal injury to determine the effects of strain and displacement rates, SAE Technical Paper, 2006.
[84] D.H. Smith, J.A. Wolf, T.A. Lusardi, V.M.-Y. Lee, D.F. Meaney, High tolerance and delayed elastic response of cultured axons to dynamic stretch injury, Journal of Neuroscience, 19 (1999) 4263-4269.
[85] M.D. Tang-Schomer, V.E. Johnson, P.W. Baas, W. Stewart, D.H. Smith, Partial interruption of axonal transport due to microtubule breakage accounts for the formation of periodic varicosities after traumatic axonal injury, Experimental neurology, 233 (2012) 364-372.
[86] P. McCrory, W. Meeuwisse, J. Dvorak, M. Aubry, J. Bailes, S. Broglio, R.C. Cantu, D. Cassidy, R.J. Echemendia, R.J. Castellani, Consensus statement on concussion in sport—the 5th international conference on concussion in sport held in Berlin, October 2016, British journal of sports medicine, 51 (2017) 838-847.
[87] S.C. Rose, A.N. Fischer, G.L. Heyer, How long is too long? The lack of consensus regarding the post-concussion syndrome diagnosis, Brain injury, 29 (2015) 798-803.
[88] D.H. Smith, W. Stewart, 'Concussion'is not a true diagnosis, Nature Reviews Neurology, 16 (2020) 457-458.
[89] J. Povlishock, D. Becker, C. Cheng, G. Vaughan, Axonal change in minor head injury, Journal of Neuropathology & Experimental Neurology, 42 (1983) 225-242.
[90] D.H. Smith, D.F. Meaney, Axonal damage in traumatic brain injury, The neuroscientist, 6 (2000) 483-495.
[91] A. Montanino, M. Saeedimasine, A. Villa, S. Kleiven, Localized axolemma deformations suggest mechanoporation as axonal injury trigger, Frontiers in neurology, 11 (2020) 25.
[92] M.T. Scimone, H.C. Cramer III, E. Bar-Kochba, R. Amezcua, J.B. Estrada, C. Franck, Modular approach for resolving and mapping complex neural and other cellular structures and their associated deformation fields in three dimensions, Nature protocols, 13 (2018) 3042-3064.
[93] R. de Rooij, E. Kuhl, Physical biology of axonal damage, Frontiers in cellular neuroscience, 12 (2018) 144.
[94] R. de Rooij, E. Kuhl, Microtubule polymerization and cross-link dynamics explain axonal stiffness and damage, Biophysical journal, 114 (2018) 201-212.
[95] A. Montanino, M. Saeedimasine, A. Villa, S. Kleiven, Axons Embedded in a Tissue May Withstand Larger Deformations Than Isolated Axons Before Mechanoporation Occurs, Journal of biomechanical engineering, 141 (2019).
[96] A. Montanino, S. Kleiven, Utilizing a structural mechanics approach to assess the primary effects of injury loads onto the axon and its components, Frontiers in neurology, 9 (2018) 643.

[97] M. Saeedimasine, A. Montanino, S. Kleiven, A. Villa, Role of lipid composition on the structural and mechanical features of axonal membranes: a molecular simulation study, Scientific reports, 9 (2019) 1-12.
[98] L.R. Frank, Anisotropy in high angular resolution diffusion ‐ weighted MRI, Magnetic Resonance in Medicine: An Official Journal of the International Society for Magnetic Resonance in Medicine, 45 (2001) 935-939.
[99] D.S. Tuch, T.G. Reese, M.R. Wiegell, N. Makris, J.W. Belliveau, V.J. Wedeen, High angular resolution diffusion imaging reveals intravoxel white matter fiber heterogeneity, Magnetic Resonance in Medicine: An Official Journal of the International Society for Magnetic Resonance in Medicine, 48 (2002) 577-582.

Appendix

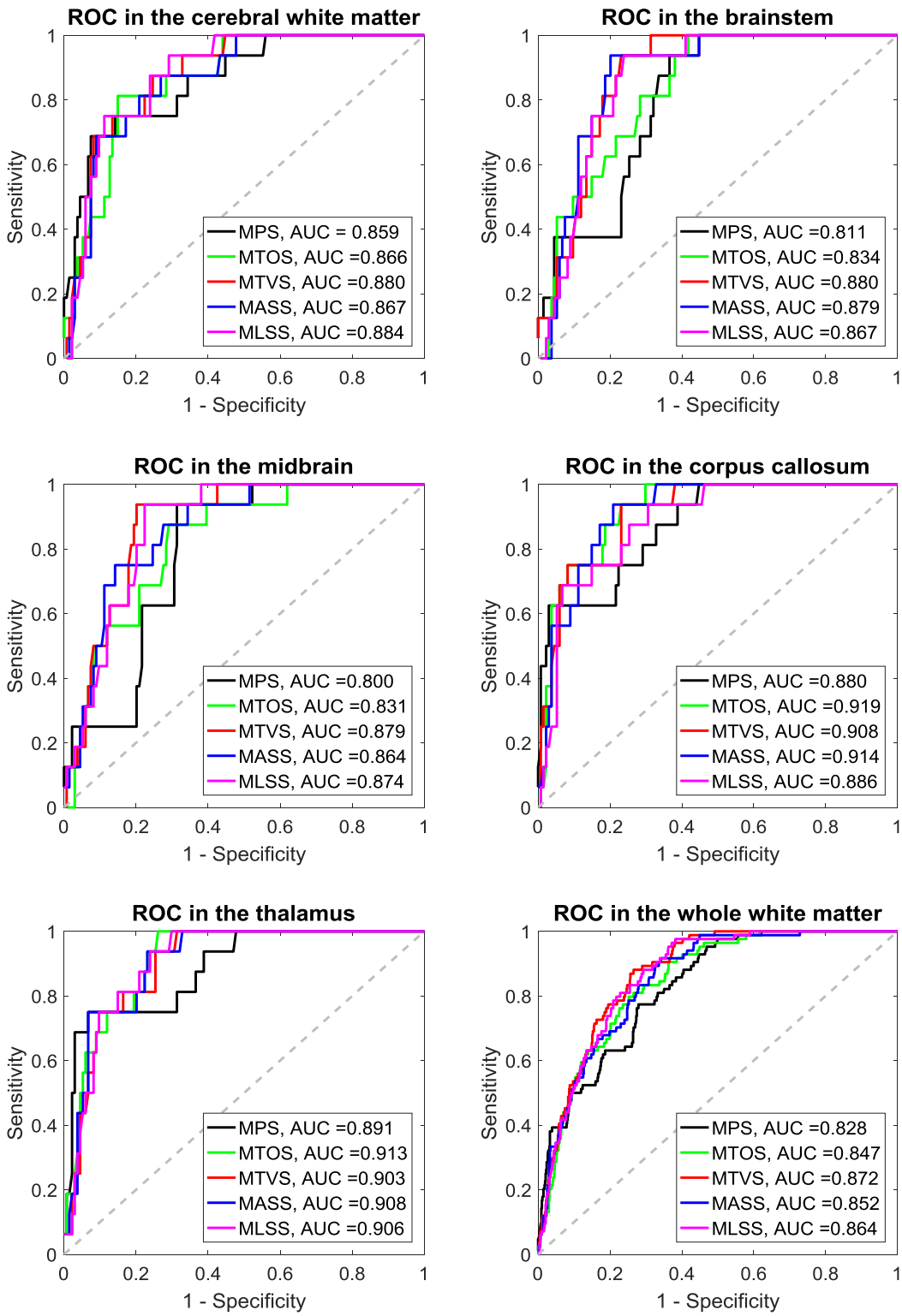

Fig. A1. Averaged receiver operator curve (ROC) for the 5 strain-based metrics in different regions of the brain based on the training datasets within the leave-one-out cross-validation framework. The area under the curve is also reported for each metrics. In each subfigure, the 50% probability line in gray dash is additionally plotted, indicating the level of a random guess (i.e., AUC=0.5).